

MICRO-MORPHOLOGICAL ANALYSES OF DIGITAL TERRAIN MODEL IN SEARCH OF TRACES OF PLOUGHING ON ARCHAEOLOGICAL OBJECTS

Izabela BASISTA¹, Ewa DEBIŃSKA^{1,*}, Krystian KOZIOL¹,
Jerzy CZERNIEC² Mateusz SOSNOWSKI³

¹Department of Integrated Geodesy and Cartography, AGH University of Science
and Technology, Al. Mickiewicza 30, 30-059 Krakow, Poland

²Institute of Archaeology and Ethnology, Polish Academy of Sciences,
Al. Solidarności 105, 00-140 Warsaw, Poland

³Wdecki Landscape Park, Rynek 11A 86-150 Osie, Poland

Abstract

The application of Airborne Laser Scanning methods (ALS) in archaeology has opened a new chapter for prospective research in forest areas. Previously, these were under-explored due to the lack of effective methods for recording archaeological remains in forests. With LiDAR data, researchers can now use available analytical tools. Also, they have developed new tools by creating so-called image derivatives, which have expanded the possibilities of microrelief interpretation for the identification of archaeological objects. This paper presents the results of DTM analyses and field investigations that were carried out at the Osie archaeological site (Poland). The site was discovered thanks to DTM analyses, which made it possible to identify an extensive settlement complex from the Late Roman Period. The object of our research was to identify remains connected with modern forest management in the form of traces of ploughing. The aim was to see how spatial data analyses, by means of which we identify ploughing traces, correlate with the results of archaeological surveys.

Keywords: ALS; DTM; Ploughing traces; Archaeology; Image filtering; Automatic detection

Introduction

The use of Airborne Laser Scanning (ALS) in archaeology has opened a new chapter for prospective research in forest areas. Previously, these were insufficiently explored due to the lack of effective methods of registering archaeological remains in forests [1–5]. Thanks to LiDAR data, researchers can now use available analytical tools [6–8]. Newly developed tools and algorithms have also expanded the possibilities of micro-relief interpretation in terms of the identification of archaeological objects, including tools such as Local Relief Modelling (LRM) [9], Sky-View Factor (SVF) [10, 11], Openness Positive and Negative [12], Topographic Position Index (TPI) [13], Morphometric Features – Minimum Curvature [14, 15], and Terrain Ruggedness Index [16]. The problem of identification of archaeological objects of different size on the basis of LiDAR surveys is related to the point cloud density and often conflicts with the conclusions of site verification, especially in forested areas. This illustrates the difficulties in unambiguous interpretation of the archaeological landscape [4]. Frequent occurrences of

* Corresponding author: ewa.debinska@agh.edu.pl

various temporal relics present in the landscape, which were interpreted as archaeological heritage, made researchers aware of the problem of landscape complexity, as the accumulation of effects of various activities and processes is reflected in micro-relief. As a result, the archaeological landscape was seen as a palimpsest. This resulted in a change of the research optics to one in which the landscape began to be understood as a complex of traces and structures that are a consequence of past human activities [17]. Furthermore, according to this line of research optics, the perceived anthropogenic features of microrelief can manifest themselves in the form of traces that are interpreted as a system of different-time phenomena. The perception of a landscape understood as a palimpsest forces researchers to adopt an approach based on a critical interpretation, which ultimately leads to the discovery and isolation of the sequence of human activities of various times recorded in the landscape. Therefore, the key step in the research process seems to be the correct identification of microrelief features, the assessment of chronology and the differentiation of possible cultural affiliations of the observed features [18].

Aim of the research

The process of landscape interpretation is definitely a task that requires proper preparation. It should be preceded by research on cartographic and historical sources. The analysis presented in this paper aimed at isolating morphological features of microrelief which occurred as a consequence of past human activities, which is a kind of landscape deconstruction. Based on induction and downsizing, the interpretation of certain phenomena visible in the landscape allows for a gradual and comprehensive understanding of the complexity of processes that took place in a given space and influenced the formation of the microrelief. It seems that in such an approach, the first proper research step should be to perform an analysis in terms of identifying traces of modern human activities related to the so-called Anthropocene [19]. The isolation of contemporary or modern traces of human activities is an excellent starting point for determining sequences of events more distant in time. Therefore, the subject of this study was the identification of remains related to modern forest management in the form of ploughing traces. The aim of the research was to check how spatial data analyses, by means of which we identify ploughing traces, correlate with the results of field studies.

So far, the interest of researchers has been focused primarily on the identification of historical objects, created as a result of a long process of ploughing. These were ridge and furrow field systems, plough headlands and others [20]. Recently, also in Poland, attention has been paid to such types of elements of archaeological sites, which should be taken into account in the process of interpretation [21]. While the above examples concerned the identification of old landscape transformations, the issue of registering modern ploughing traces still remains open. In this article, we try to diagnose the problem of identifying traces of forestry within archaeological sites. It was assumed that such identification is important not only in the process of deconstruction and isolation of landscape features but is also significant from the point of view of conducting prospective and verification studies in the field. The results of analyses showing the traces of ploughing may be helpful in terms of research planning and assessing its effectiveness in difficult forest terrain. Therefore, it was decided to check how the identification of zones with traces of modern forest ploughing, occurring within archaeological sites with microrelief, affects the research process.

This article presents the results of DTM analyses and field research carried out at the Osie archaeological site. The site was discovered thanks to DTM analyses, which made it possible to recognise an extensive settlement complex from the Late Roman Period [22]. It consists of a complex of embankments interpreted as mid-field balks (Fig. 1) and a residential and production settlement with a road relic (Fig. 2). The complex includes relics of fields, roads, barrows and a settlement located in the centre. This unique find of a completely

preserved rural landscape forced researchers to develop a new approach of investigation. In the first place, attention was drawn to the need of identifying areas with traces of ploughing, because, as shown by the experience of surface surveys in agricultural areas, ploughing causes historic features to be thrown onto the surface [23]. The current results of excavations in forest areas indicate a shallow occurrence of cultural layers, often just under a very thin layer of undergrowth. On the one hand, this intensifies the destruction process, on the other hand, it gives a chance for a possible registration of artifacts on the surface.

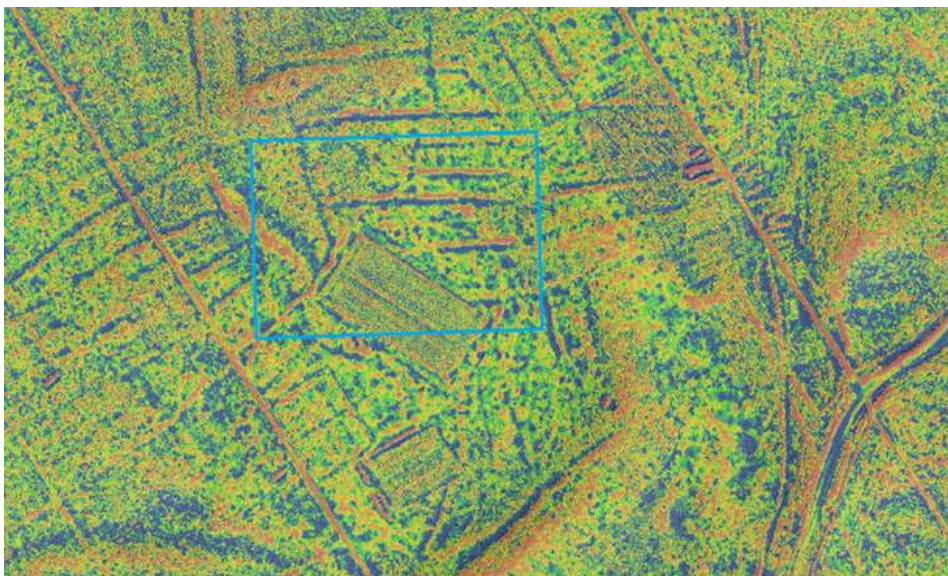


Fig. 1. Mid-field balks from the Late Roman Period

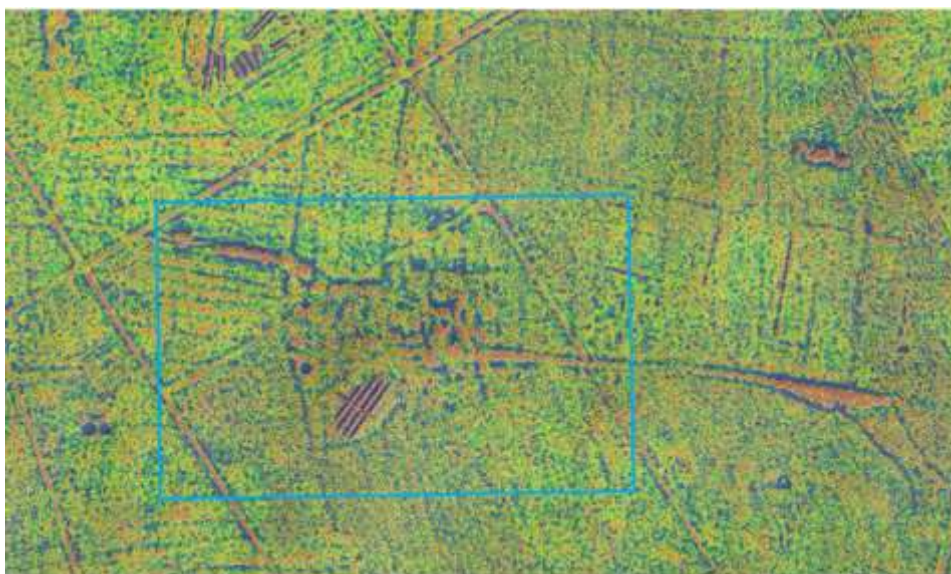


Fig. 2. A residential and production settlement with a relic of a road running horizontally in the central part of the image

The first stage of the research was to determine the most effective DTM analysis which would allow us to clearly identify ploughing traces in order to select areas for prospective research. Six analyses were selected for this purpose: Local Relief Model (LRM) [9, 24, 25], Sky-View Factor (SVF) [10, 11], Openness Positive (OPEN_POS) and Openness Negative (OPEN_NEG) [11, 12, 26], Topographic Position Index (TPI) [27–29], Morphometric Features - Minimum Curvature (MIN_CURV) [14, 15], and Terrain Ruggedness Index (TRI) [16]. The following research questions were posed: which of the analyses provide satisfactory images for unambiguous identification of ploughing traces? Whether, and how, the images obtained allow for the assessment of the degree of destruction occurring at archaeological sites and can they be helpful in planning field research? Can the results of the above analyses support the process of interpreting positions?

Currently, research on ploughing traces based on DTM is being conducted to detect arable soils for the purpose of classifying agricultural lands [30]. In archaeology, the problem of the presence of traces of modern ploughing at sites is perceived as noise, as a factor disturbing the process of identifying objects with an older metric [31]. In this article, we take the opposite approach and treat the identification of ploughing traces as the key information for the research questions.

Study area

The study covered a forest area of over 200ha in the Wdecki Landscape Park, which is the eastern part of the Bory Tucholskie forest complex in northern Poland (Fig. 3). It is a very old forest complex with a diverse age structure of the stand. Within the research area, there are deciduous and mixed forests, where a mean age of trees are 130-170 years old. On a map from the beginning of the 19th century, the research area is shown as heavily forested (Fig. 4). On this basis, it was concluded that in modern times only forestry was carried out there. The starting point for the research was a comprehensive DTM analysis, the purpose of which was to identify archaeological objects occurring in the Wdecki Landscape Park. As a result, two archaeological sites - test fields - were selected for the purpose of identifying traces of forest ploughing.

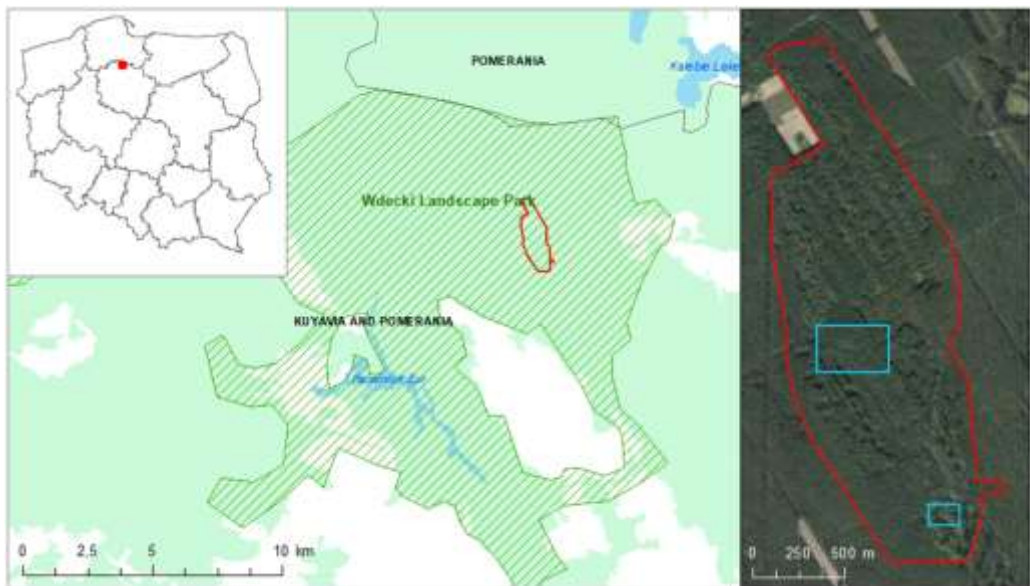


Fig. 3. Red outline - location of the study area, blue - upper and lower test fields
(source: BDOO, geoportal.gov.pl)

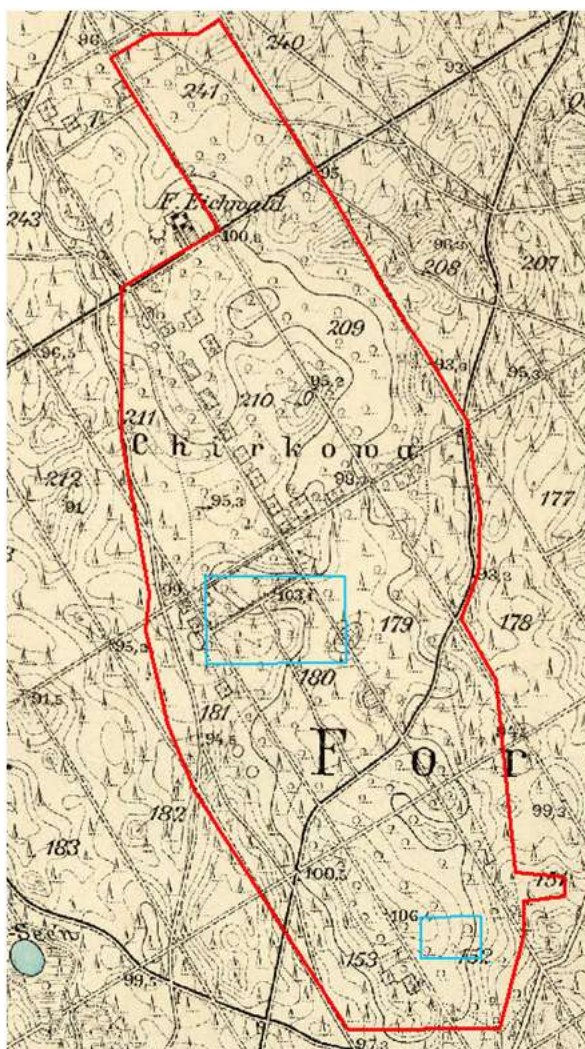


Fig. 4. Location of the study area (red) on the map from 1910, blue - upper and lower test fields [32]

Materials and Methods

LiDAR ISOK data description

In Poland, ALS research has been conducted as a part of the ISOK project [33]. ALS data gathered during the ISOK project covers more than 90% of the Polish territory. These data can be classified into standards (Standard I and Standard II) based on the parameters included in Table 1. Currently, LiDAR datasets can be downloaded from the National Geodetic and Cartographic Resource. They are used in numerous research projects by specialists in various domains, as they are the first remote sensing data on terrain relief of such accuracy. This is particularly important in areas covered with trees. Mountain terrains are included in Standard I (Table 1). Other values that characterise ALS standards were not summarised in Table 1, as they do not demonstrate significant changes between the standards and do not affect the accuracy of LiDAR-based elevation data.

Table 1. Characteristics of the ISOK LiDAR products with regard to standards

Parameter	Standard I	Standard II
Point cloud density	≥ 4–6 pts/m ²	≥ 12 pts/m ²
Vertical accuracy (mean error) of the ALS point cloud after alignment (on flat, paved surfaces)	mh ≤ 0.15m	mh ≤ 0.10m
Horizontal accuracy (mean error) of the ALS point cloud after alignment (on flat, paved surfaces)	mp ≤ 0.50m	mp ≤ 0.40m
Term of measurement	From October to the end of April	Entire year

The point cloud was assigned the following numerals during classification:

1. Points processed but not classified.
2. Ground points.
3. Points representing low vegetation, i.e., between 0 and 0.40m.
4. Points representing medium vegetation, i.e., between 0.40 and 2.00m.
5. Points representing high vegetation, i.e., higher than 2.00m.
6. Points representing buildings, structures and engineering objects.
7. Noise.
8. Points representing underwater areas

Measurement data of ALS ISOK are stored and made available in the system of topographic map division in the scale of 1:5.000. The analysed area was present on six map sheets (N34-85-Ba-222, N34-85-Ba-224, N34-85-Ba-242, N34-85-Bb-111, N34-85-Bb-113, N34-85-Ba-131), which were downloaded from geoportal.gov.pl. SAGA GIS software was used to process LAS files. In the first stage, *Ground* points (class 2) were extracted from the point cloud by using the Point Cloud Reclassifier/Subset Extractor module. Then, the point cloud was converted to a grid form with a given resolution in the Point Cloud to Grid module, with Aggregation set as mean value, and the Cellsize = 0.25. In the next step, *No data* values were eliminated in the Close Gaps module, with the Tension Threshold = 0.1. As a result, the Digital Terrain Model (DTM) with a cell size of 0.25m was obtained using the Nearest Neighbourhood algorithm.

By processing the DTM with LRM, SVF, OPEN_NEG, OPEN_POS, TRI, TPI and Minimum Curvature algorithms, seven images derived from the DTM were obtained. The resulting images were described in terms of the visibility of ploughing traces and then compared by creating profiles at five selected field locations. The results of automatic detection of plough traces on each of the derived images are also presented. The quality of the classification was evaluated and the best DTM-derived image for automatic detection of plough traces was identified.

Digital Terrain Model derivatives

The algorithms Local Relief Model, Sky-View Factor, Openness Positive and Negative, Topographic Position Index, Morphometric Features - Minimum Curvature and Terrain Ruggedness Index were used to generate DTM derivatives. The description of each algorithm and the presentation of their most important parameters are provided below. 30-meter-long profiles located in five characteristic places of the study area were used to identify appropriate values of parameters (Fig. 5a and c). The obtained images were compared by analysing two test fields - the upper one (Fig. 5b) with dimensions of about 400×250m and the lower one with dimensions of about 200×100m (Fig. 5d).

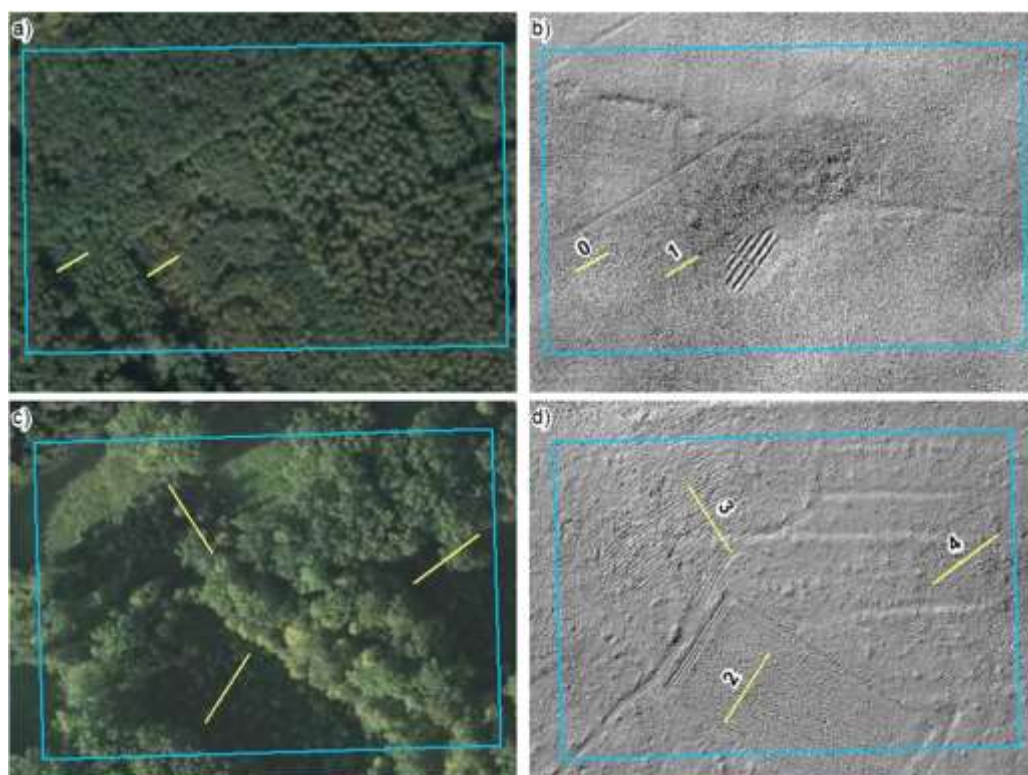


Fig. 5. Field cross-sections (yellow) on a high-resolution orthophotomap on the upper (a) and lower (c) test field. Field cross-sections (yellow) on the analytical hillshading 315 degrees and 35 degrees on the upper (b) and lower (d) test field

Local Relief Model (LRM)

Local Relief Model (LRM) was developed for mountainous regions and produces a model in which macrotopography is reduced while retaining the integrity of microtopography [9]. The LRM image was created using a tool implemented in the ArcGIS environment [34] by applying the following steps:

1 Using low pass filters on the DTM. The parameters to choose from were: [a] Neighbourhood: Circle, Rectangle, Annulus, Wedge, Irregular, Weight; [b] Size of the mask in pixels or map units; [c] Statistic Type: mean, mix, min, std, range, sum.

The smoothed height model (SHM) is the first approximation of large-scale landscape forms. The mask size of a low pass filter determines the size of features that will be highlighted in the LRM. Thus, assuming the distance between the plough ridges to be 1.25 – 1.50m, the mask size of 5 pixels was used at first.

2 Computing Digital Model (DM) by subtracting the SHM from the DTM. By subtracting the smoothed height model from the DTM, the first approximation of local relief is obtained: only minor morphological features are retained in the model, while large-scale topographic forms are eliminated.

3 Extracting the $h = 0$ contour from DM, the result is DM0.

4 Extracting the height from the DTM, coinciding with the DM0, creating a simplified Surface DTM, (simplified Surface = purged DTM), interpolating the final LRM.

This processing step creates a cleared DTM from the DTM points along the contour lines for which height $h = 0$ in the LRM. The result is the so-called cleaned DEM that represents large-scale landscape forms after eliminating small terrain forms. The final LRM is the result of

subtracting this refined DTM from the original DTM. The resulting LRM reflects information about the heights of small-scale objects in relation to the entire landscape.

The LRM algorithm is used to detect local changes by examining the nearest neighbourhood. It highlights local field differences with the rejection of large morphological forms. By applying the above steps, small off-road forms are sharpened. According to Kiarszys and Banaszek [35], the LRM method works well for detecting convex objects, such as embankments or burial mounds.

Parameterisation of the shape and size of the mask as well as statistics were carried out in the conducted research.

Considering the shape of the mask with the following sizes, rectangle - size 5, circle - radius 2, and annulus with parameters 1, 3, the derived images give very similar results in a visual evaluation, which can be seen in the profiles (Figs. 6 and 7). The rectangle mask was selected for further analysis. Regarding the calculation of the mask size, in the case of circle and annulus it is $1 + 2R$, where R is the radius, so in the presented examples (Figs. 6 and 7) all types of masks have similar search areas.

However, if we take into account the size of the rectangle mask (Figs. 8 and 9), i.e., the side with a length of 2.5 or 10 pixels, large amplitudes can be noticed for the side of 10 pixels long.

The change of statistics between mean, mix, min, std, range, sum did not result in significant differences in the tested area.

To sum up the analysis on the LRM, an image with the following parameters was selected for further comparisons: rectangle-shaped mask with a side of 10 pixels, statistics type: mean.

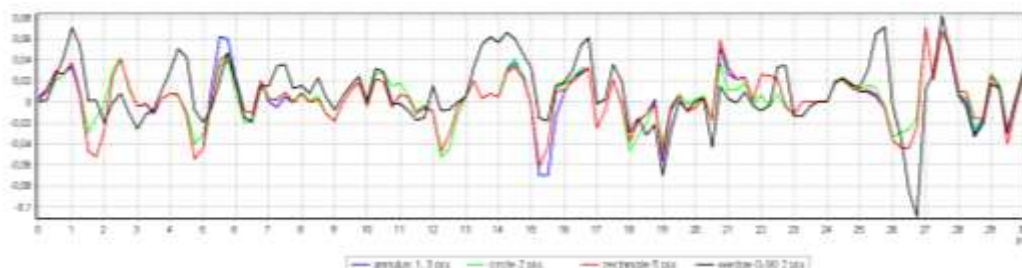


Fig. 6. Sample profiles (id = 0) on LRM images for the same search radius ~ 5 pixels with different masks: annulus (radii = 1.3 pixels), circle (radius = 2 pixels), rectangle (side = 5 pixels) and wedge (starting angle = 0° end angle = 90°, radius = 2 pixels)

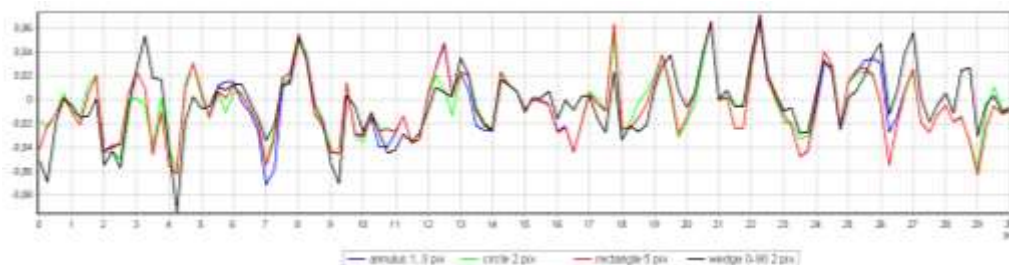


Fig. 7. Sample profiles (id = 1) on LRM images for the same search radius ~ 5 pixels with different masks: annulus (radii = 1.3 pixels), circle (radius = 2 pixels), rectangle (side = 5 pixels) and wedge (starting angles = 0° end angle = 90°, radius = 2 pixels)

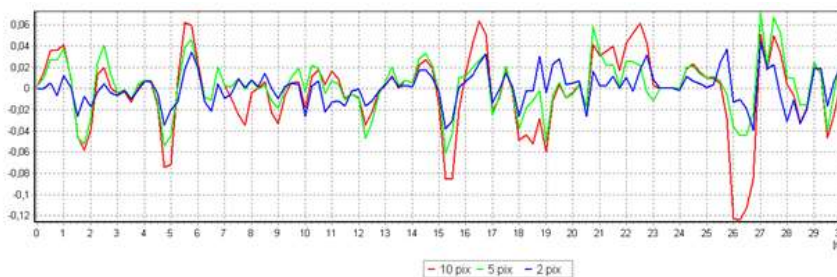


Fig. 8. Sample profiles (id = 0) on LRM images for the same mask – rectangle with a different side length: 10,5 and 2 pixels

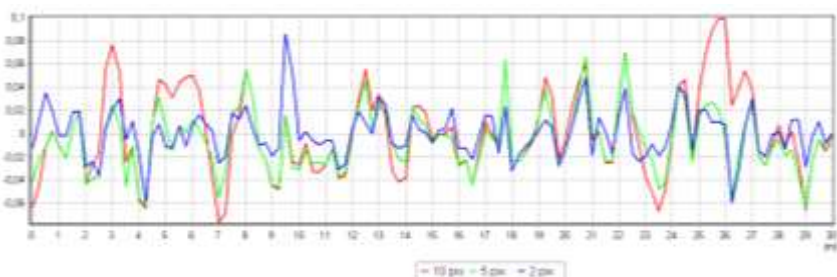


Fig. 9. Sample profiles (id = 1) on LRM images for the same mask - rectangle with a different side length: 10, 5 and 2 pixels.

Sky-View Factor (SVF)

The Sky View Factor (SVF) is a parameter that measures the portion of the sky visible from a certain point [11]. It is determined by the formula (1) [36]:

$$SVF = 1 - \frac{\sum_{i=1}^n \sin \gamma_i}{n} \tag{1},$$

where: γ is the vertical angle of the relief horizon in the specified direction, n is the number of directions used to estimate the vertical angle of the relief horizon.

The SVF ranges between 0 and 1. It is calculated for the specified range (r) – search radius. If there is no obstacle disturbing the visibility of a given point within the defined range (r), then the value is the largest and equals 1. Each element interfering with the visibility of hemisphere causes a decrease in this value. In the visualisation of the results of this analysis, flat areas, ridges or peaks appear in light colours, and depressions are dark because less sky is visible. In this method, due to calculations only for angles above the virtual horizon, concave forms are reflected much better than convex forms.

The results of this analysis are completely shadowless because there is no directional illumination. The hemisphere is assumed to be equally bright throughout its area. As a result, it is impossible to understand altitude relations in the study area. However, this only applies to large geomorphological structures. In their case, when analysing the results, it is necessary to use other methods of visualisation, or a height measurement is needed [35].

The main parameters that influence the SVF-based relief visualisation are the number of horizon search directions and the maximum search radius. Taking into account the shape of the searched objects (ploughing traces), where the distances between the ploughing furrows is about 1.5 meters, it was decided that the search radius would be 5 pixels, i.e., 1.25 meters. This choice is confirmed by the profiles (Fig. 10). The largest amplitudes and the clearest furrows are visible in the SVF image with the smallest search radius. Following the suggestions of Zaksek [11] and Dozier [37] as well as the analyses of profiles (Fig. 11), 8 horizon search

directions were applied. Additionally, the examined image was also denoised, i.e., individual pixels that are usually the result of data collection or processing were removed. It was found that when testing such small forms, these single pixels may distort the results. The SVF visualisation was made using a Relief visualisation Tool [10, 11].

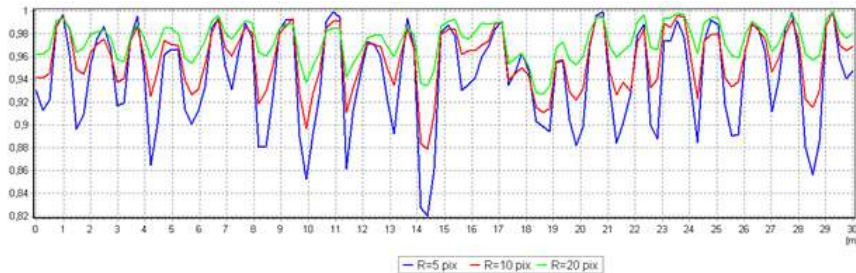


Fig. 10. Sample profiles (id = 2) on SVF images for the same number of horizon directions = 8, with a different search radius of 5, 10 and 20 pixels



Fig. 11. Sample profiles (id = 2) on SVF images for the same search radius = 5 pixels with a different number of horizon directions - 32, 16 and 8 directions

Openness Positive and Negative (OPEN_POS/OPEN_NEG)

The openness technique computes two vertical angles for each pixel: the first one - relative to the zenith, the other one - to the nadir [38]. The angles are calculated on terrain profiles derived from a tested point, along at least eight directions (N, NW, W, SW, S, SE, E, NE) within the assumed search radius. Starting from the pixel under consideration, the greatest possible zenith or nadir angle is determined along each profile [12]. Unlike SVF, these activities are not limited by the horizon. The mean value of all angles relative to the zenith is positive openness, and the averaging of the angles relative to the nadir is negative openness. The obtained values may theoretically vary from 0° to 180° . When interpreting the results, in the Openness Positive images, small values of angles relative to the zenith indicate concave forms, while in the Openness Negative images, small values of angles relative to the nadir indicate convex forms. Perfectly flat surfaces, whether horizontal or inclined, have opening values of 90° [12]. A very important parameter in this method is the search radius. It determines which topographic elements will be ignored when calculating the openness value for a specific location. With small search distances, local microtopographic differences will increase, with a large search radius (several hundred meters), river valleys and hill tops will be emphasized [35].

Taking into account the objects studied in this paper and having analysed the profiles (Figs. 12 and 13), a search radius of 5 pixels, i.e., 1.25 meters, and 8 search directions were selected.

The openness visualisation was made using a Relief visualisation Tool [10, 11].

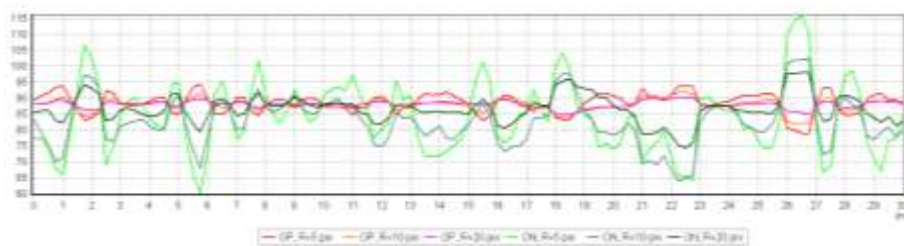


Fig. 12. Sample profiles (id = 0) on Openness Positive (OP) and Openness Negative (ON) images for the same number of horizon directions = 8, with a different search radius - 5, 10 and 20 pixels.

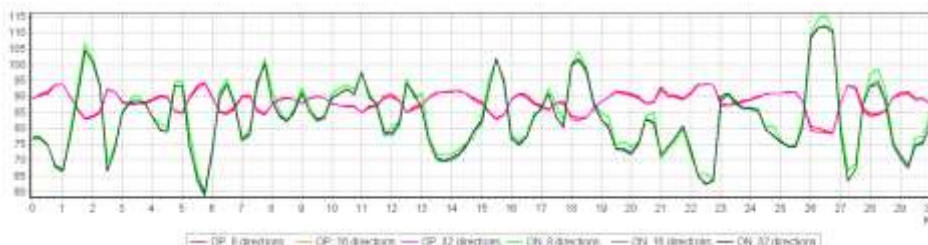


Fig. 13. Sample profiles (id = 0) on Openness Positive (OP) and Openness Negative (ON) images for the same search radius = 5 pixels with a different number of horizon directions - 8, 16 and 32 directions

Topographic Position Index (TPI)

The Topographic Position Index (TPI) compares the value of height assigned to a given cell to the mean value calculated for the previously determined neighbourhood of this cell [13], according to the formula (2) [29]:

$$TPI_i = M_0 - \sum_{n-1} M_n / n \quad (2),$$

where: M_0 = elevation of the model point under evaluation, M_n = elevation of a grid, n = the total number of surrounding points included in the evaluation.

The shape of the neighbourhood can be any: rectangle, circle, ring, wedge, or custom.

The calculations presented above can give positive or negative values. Cells for which a $TPI > 0$ are higher than the tested neighbourhood, and those with a $TPI < 0$ are lower than the tested neighbourhood. Due to the fact that the tested elements - traces of plough furrows - are about 1.5m in size, in the case of other options, the mask size was 5-7 pixels.

The analysis was done in SAGA GIS 7.9.0 where mask selection is limited to circle and annulus. In addition, the distance weighting function had to be selected with the following parameters: [0] - no distance weighting, [1] - inverse distance to a power, [2] - exponential, [3] - Gaussian.

First, different types of masks were tested, with different parameters. Then, the masks were checked in all variants of distance weighting. Selected results are shown below.

From the graph (Fig. 14) it can be seen that the greatest amplitudes occur with the annulus mask with radii 1, 3, and with the Gaussian distance weighting option, bandwidth: 1. A comparison of different methods of weighting distances for the annulus mask with radii 1, 3 can be seen in figure 15, then the situation repeats itself, Gaussian, bandwidth: 1. can be distinguished.

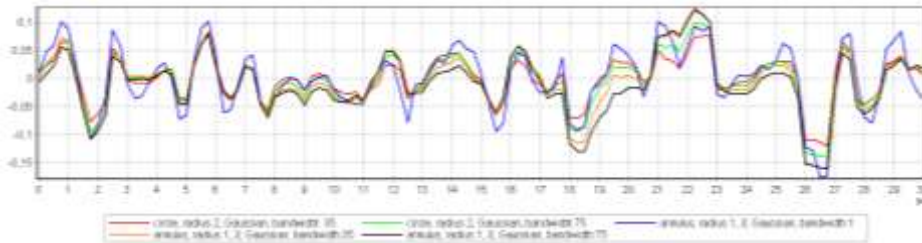


Fig. 14. Sample profiles (id = 0) on TPI images for the mask (red) circle, radius = 2, Gaussian distance weighting, bandwidth: 35 (green) circle, radius = 2, Gaussian distance weighting, bandwidth: 75 (blue) annulus, radii = 1, 3, Gaussian distance weighting, bandwidth: 1 (orange) annulus, radii = 1, 3, Gaussian distance weighting, bandwidth: 35 (black) annulus, radii = 1, 3, Gaussian distance weighting, bandwidth: 75

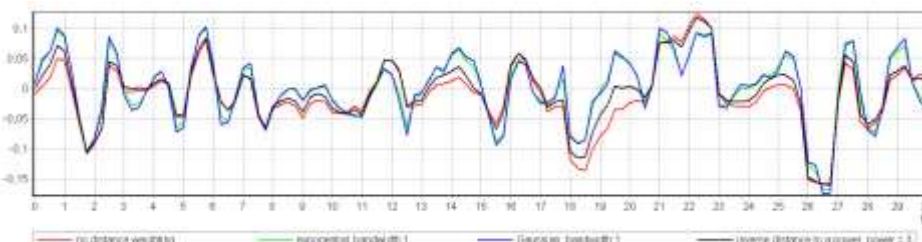


Fig. 15. Sample profiles (id = 0) on TPI images for the annulus mask, radii = 1, 3, for various distance weighting function options; (red) no distance weighting (green) exponential, bandwidth: 1 (blue) Gaussian, bandwidth: 1 (black) inverse distance to a power, power = 3

Taking into account the results of TPI analyses, the TPI image created based on the annulus mask of radii = 1, 3, Gaussian distance weighting, bandwidth: 1 was selected for further comparisons.

Morphometric Features - Minimum Curvature

The curvature map calculates the relative change in slope and can be viewed as the value of the second order derivative of DEM at a point. Numerous equations and definitions can be found in the literature, but both definitions and equations often contradict each other. For example, "plan curvature" is defined as the curvature of a cross-section of a landscape intersecting the XY plane or the curvature of a plane intersecting the plane of normal slope and perpendicular to the direction of slope. Some sources add negative signs to the equations, thus reversing the signs of the curvature values, while others do not. There are three methods commonly used to calculate curvature from raster elevation models. The first one was proposed by Evans [39], the second method proposed by Zevenbergen and Thorne [40] and the third method proposed by Shary [41].

ArcGIS Spatial Analyst uses Zevenbergen and Thorne's method while SAGA GIS and LandSerf use the Evans approach. The solution proposed by Shary [41] has not been implemented in any software but its results are very close to the Evans method [42]. All approaches use a moving 3x3-cell window and calculate the curvature based on 9 raster cells in the window. The difference between the approaches is the use of a different polynomial parameterisation, the Evans approach fits the curve to 9 elevation points using a 6-parameter polynomial [39], while Zevenbergen and Thorne's method uses a 9-parameter polynomial. Florinsky [43] favours the Evans approach because it filters out small random errors in the original DEM compilation. Florinsky [44] also shows mathematically that the Evans' method is more precise than the Zevenbergen & Thorne method [45] argues that quadratic-based algorithms (such as the Evans method) are more stable than partial quadratic-based algorithms such as Zevenbergen & Thorne's. GIS systems typically offer the calculation of 7 types of landscape curvature as a complete characterisation of the landscape [14]:

- profile convexity (intersecting with the plane of the Z axis and aspect direction);
- plan convexity (intersecting with the X Y plane);
- longitudinal curvature (intersecting with the plane of the slope normal and aspect direction);
- cross-sectional curvature (intersecting with the plane of the slope normal and perpendicular aspect direction);
- maximum curvature (in any plane);
- minimum curvature (in any plane);
- mean curvature (in any plane).

Taking into account the data and the goal of obtaining the discriminant of minimum differences, in this case only the result for Morphometric Features - Minimum Curvature should be considered. The minimum curvature is measured perpendicularly to the direction of the maximum curvature. The maximum curvature is measured in any direction. The minimum curvature is calculated on the basis of (3):

$$\text{prof}_{c_{MIN}} = -a - b - \frac{((a - b)^2 + c^2)^{\frac{1}{2}}}{2} \quad (3)$$

where: a, b, c - are the coefficients of the polynomial.

In the experiment, the Evans model was used in a large-scale approach by adjusting square parameters to a window of any size. This is the method proposed by Jo Wood [14] and implemented in LandSerf, GRASS and SAGA GIS.

In the experiment, kernel values of 3, 5, 7, 9 and 11 were examined, the results of which for the examined areas are presented in graphs (Figs. 16 and 17).

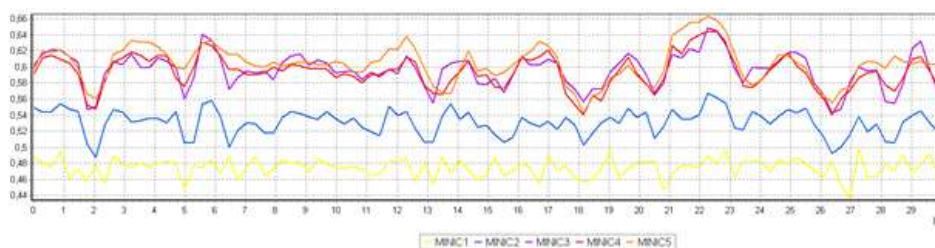


Fig. 16. Sample profiles (id = 0) in Minimum Curvature images for the kernel value: 3 - yellow (MINIC1), 5 - blue (MINIC2), 7 - purple (MINIC3), 9 - red (MINIC4) and 11 - orange (MINIC5)

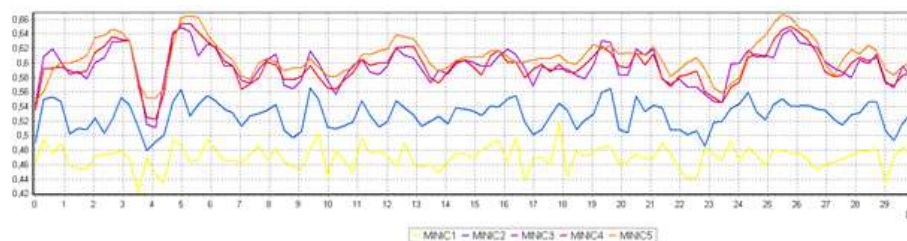


Fig. 17. Sample profiles (id = 1) on Minimum Curvature images for the kernel value: 3 - yellow (MINIC1), 5 - blue (MINIC2), 7 - purple (MINIC3), 9 - red (MINIC4) and 11 - orange (MINIC5)

Using the Morphometric Features - Minimum Curvature analysis, the use of a small kernel (Fig. 16 and 17/MINIC1) on selected test objects turned out to expose noise. However, kernels with values from 7 pixels to 11 (Fig. 16 and 17/MINIC3, MINIC4, MINIC5) generated similar responses in both cases. For these values, an increase in local minima and local maxima, and a smoothing of the values in between can be observed. This confirms the assumption that increasing the kernel value in this analysis is not advisable for the detection of the microrelief. As can be seen from the graphs (Fig. 16 and 17) in terms of variation of amplitude and variation

of values characterising the microrelief, the result obtained for a kernel equal to 5×5 pixels is satisfactory (Fig. 16 and 17/MINIC2).

Terrain Ruggedness Index (TRI)

The Terrain Ruggedness Index (TRI) is a measure developed by Riley et al. [16], which expresses the magnitude of difference in elevation between adjacent cells of a digital elevation grid model. The process calculates the difference in elevation values between a central cell and the eight surrounding cells. Then, all height difference values are squared in order to obtain positive values, which are then averaged. The terrain ruggedness index is derived by the square root of the averaged value and corresponds to the average change in height between any point on the grid and the surrounding area. The TRI expresses the difference in elevation between adjacent cells of a digital elevation grid (4).

$$\rho = \gamma \left[\sum_{j=1}^n (x_{i,j} - x_{0,0})^2 \right]^{1/2} \quad (4),$$

where: i, j is the max cell size and 0,0 is the min. cell size in processed data of the elevation value.

The Terrain Ruggedness Index (TRI) is a secondary geomorphometric parameter used to describe and quantify local relief. *M. Różycka et al.* [46] investigated its usefulness in geomorphological studies of landslides; the TRI proved to be capable of differentiating landslide populations into smaller groups. The TRI is applied in studies of catchments of water, with different roughness characteristics, located in mountainous areas [47]. The TRI is most commonly used in studies of surface roughness identifying typical morphological features that may reflect mass deposition of gravity flow (landslides and movement of earth masses) [48, 49]. In a planned study on the detection of modern traces of forest ploughing by studying micro-morphological changes, the TRI was investigated using SAGA GIS. The implemented TRI algorithm requires the following parameters: search mode, search radius, weighting function. The search radius is the metric distance of the index action, and search mode defines a square or circular shape for the action area of the function calculation. The last factor controls the distance weighting calculation method and can take values: [0] - no distance weighting, [1] - inverse distance to a power, [2] - exponential, [3] - Gaussian.

An analysis of the variation of the Search Mode parameter was performed for sample areas, where 0 indicates a square neighbourhood and 1 indicates a Circle neighbourhood. The analysis showed that identification of ploughing traces would be more effective if the Search Mode parameter = 1, i.e., in the analysis of the Circle surroundings.

The analysis showed no significant changes with different values of the Weighting Function parameter. Available choices are: [0] no distance weighting, [1] inverse distance to a power, [2] exponential, [3] Gaussian.

The search radius parameter is an integer value of cells. In SAGA GIS, this parameter is calculated according to the formula: 1+2* radius given as a number of cells in a kernel. The results of the analyses are illustrated by cross-section profile for sample lines (Figs. 18 and 19).

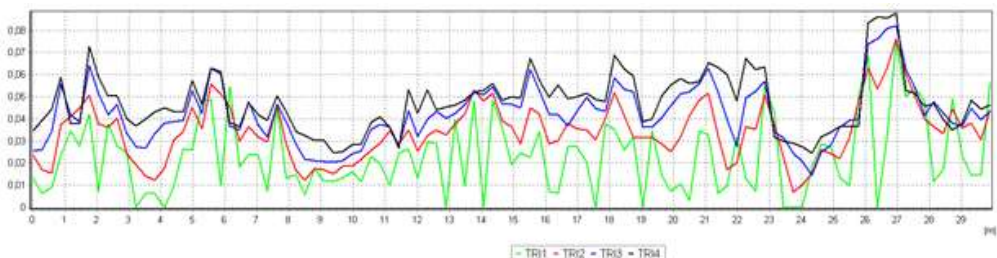


Fig. 18. Sample profiles (id = 0) in TRI images for kernel values: 3 - green (TRI1), 5 - red (TRI2), 7 - blue (TRI3), 9 - black (TRI4)

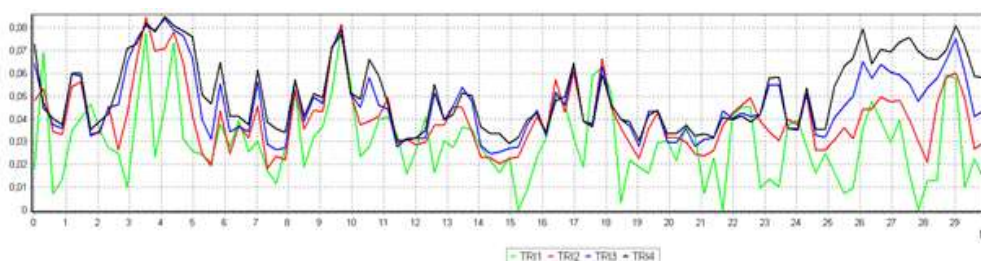


Fig. 19. Sample profiles (id = 1) in TRI images for kernel values: 3 - green (TRI1), 5 - red (TRI2), 7 - blue (TRI3), 9 - black (TRI4)

By analysing the values obtained for the Terrain Ruggedness Index (TRI) analysis, in which the kernel value was the main differentiating component of the results obtained, extreme values can be rejected in advance. With the smallest kernel, the amplitude is large but the noise value is also very high. This will result in detecting large overestimates of ploughing traces and detecting them in places where they do not exist. On the other hand, the value of the maximum kernel works exactly in the opposite way, the black line in the graphs (Fig. 18 and 19) is smoother. Given the other results, it is hard to clearly indicate a better solution. The field survey allowed us to decide that the 7x7 kernel is the most suitable one.

Results

Algorithm for testing the results of parameterisation of DTM derivatives

As a result of the tests, suitable parameters were selected for each algorithm. The table below presents a list of the tested algorithms along with the adopted parameters which showed the highest amplitudes on the tested profiles (Table 2).

Table 2. The list of analysed algorithms with adopted parameters

Algorithm	Search radius	Other parameters
Local Relief Model	10 pixels	Search Mode = rectangle
Sky-View Factor	5 pixels	Search Directions = 8
Openness positive	5 pixels	Search Directions = 8
Openness negative	5 pixels	Search Directions = 8
Topographic Position Index	7 pixels	Search Mode = annulus
		Weighting Function = Gaussian, bandwidth: 1.
Minimum Curvature	5 pixels	
Terrain Ruggedness Index	7 pixels	Search Mode = circle,
		Weighting Function = no distance weighting

Seven output images (DTM derivatives) were obtained and compared with each other. First, a visual comparison of the images was made. Then, the profiles generated along 5 test lines were compared (Fig. 5). The resulting images were also subject to automatic detection based on morphological filters in order to detect traces of ploughing.

Visual comparison

In our study, seven DTM derivatives were compared visually. Bright pixels in the pictures show terrain elevations, while dark ones show depressions.

In the upper test field (Fig. 5a and b), there are drainage ditches in the depression, and traces of ploughing around them. One strip of field (clearer) runs from the north-west to the south-east (left side of the photo), and another strip of field (less distinct) runs from the north-east to the south-west (right side of the photo). The latter ploughing traces can be characterised by shallower and not so parallel furrows as in the case of the first strip of the cultivated field. In each of the examined images, these two characteristic traces of furrows are visible. Starting

with the best image, the most distinct traces of ploughing appear in the SVF image (Fig. 20b), however, in some places they were disturbed by depressions from this area. The next two pictures, Openness Positive (Fig. 20c) and Openness Negative (Fig. 20d), also show traces of ploughing very clearly. These images are less contrastive compared to the SVF, but larger terrain forms (depressions) have been eliminated so that ploughing traces are clearly visible throughout the test field. The LRM image (Fig. 20a) has a similar contrast to OPEN_POS and OPEN_NEG but is also disturbed by the appearance of depressions. Clear depressions, the bottoms of the furrows, can be seen in the MIN_CURV image (Fig. 20e), they are very contrasting, but the tops of the furrows are very blurred. The TPI image has low contrast, hence ploughing traces are not as clearly visible as in, for example, OPEN_NEG/POS. It is the most difficult to find traces of arable fields in the TRI image. Only the tops of furrows can be recognised there. Although this image has high contrast, larger terrain forms, such as drainage ditches or depressions are better detailed here.

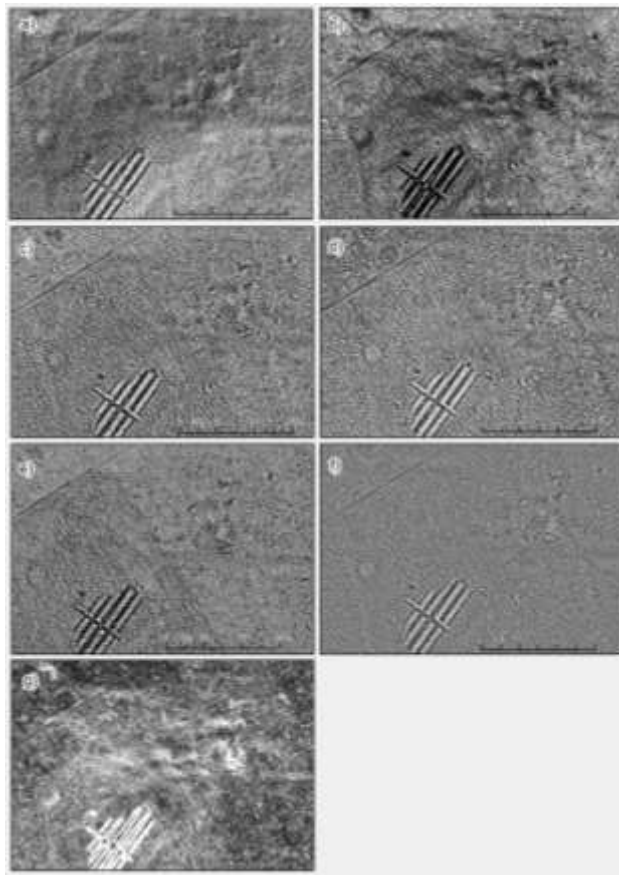


Fig. 20. Upper test field visualisation: a) Local Relief Model, b) Sky-View Factor, c) Openness Positive, d) Openness Negative, e) Minimum Curvature, f) Topographic Position Index, g) Terrain Ruggedness Index

In the lower test field (Fig. 5c and d) there are three arable fields. The first one - in the north-west, the second one - in the south, and the third one - in the east. The central field (in the south) has the most regular shape - straight parallel lines and the deepest furrows, the remaining fields are characterised by shallower and wavy furrows. In each of the DTM derivatives, these three fields are visible. As in the case of the upper test field, the most visible traces of arable

fields are in the SVF image (Fig. 21b). Field bays from the times of Roman influence are clearly visible there - three horizontal stripes running on the eastern side of the test field. The plough furrows are also clearly visible in the OPEN_POS and OPEN_NEG images (Fig. 21c and d). Additionally, in the OPEN_NEG image, the ridges of the furrows are wider and more visible. In the LRM, MIN_CURV and TPI images (Fig. 21a, e and f), arable fields are similarly recognisable. It is the most difficult to recognise traces of farmland in the TRI image (Fig. 21g).

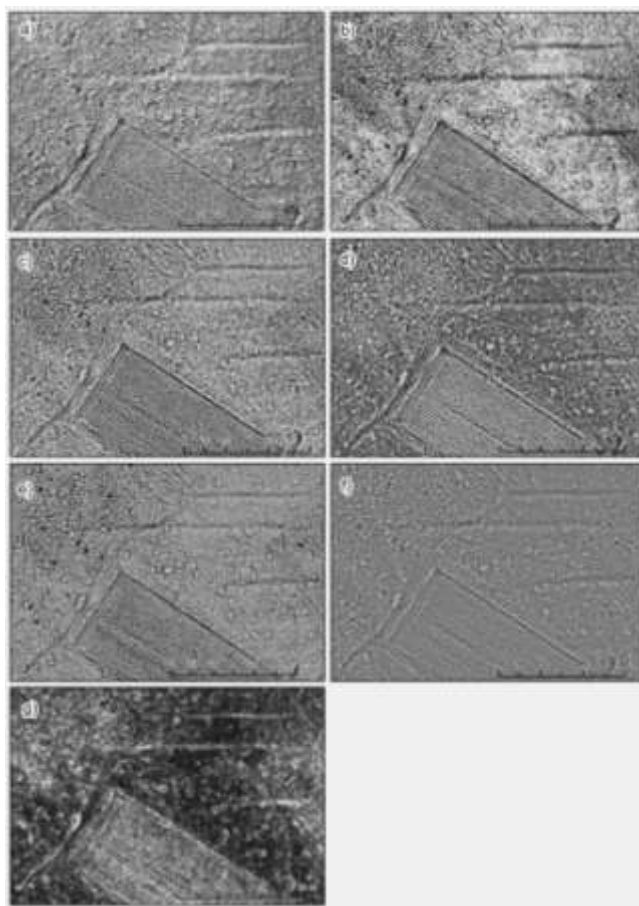


Fig. 21. Visualisation of the lower test field: a) LRM, b) SVF, c) Openness Positive, d) Openness Negative, e) Minimum Curvature, f) Topographic Position Index, g) Terrain Ruggedness Index

Cross-section amplitude testing

The resulting images were compared with each other using profiles generated along five test lines. The profiles were made on images which were first standardised and normalised. Standardisation activities were performed in SAGA according to the following steps:

Step 1. Standardising the values of a grid. The standard score (z) (5) is calculated as a raw score (x) less arithmetic mean (m) divided by a standard deviation (s).

$$z = (x - m) / s \quad (5)$$

Step 2. Normalising the values of a grid. Rescaling all grid values to fall in the range from 0 to 1.

Pixels in normalised images have values ranging from 0 to 1 and an expected mean value of 0, and a standard deviation of 1. Values oscillating close to 0 show depressions of the

terrain, while values of about 1 show elevations. The exception is the visualisation of negative openness, where values close to 0 mean elevations, and values close to 1 mean lower terrain.

The profiles were made in five characteristic places of the study area (Fig. 5). Each of the profiles were about 30 meters long. Four profiles with the identifier's id = 0, id = 1, id = 3, and id = 4 were made in places where, during field research, traces of ploughing were poorly visible.

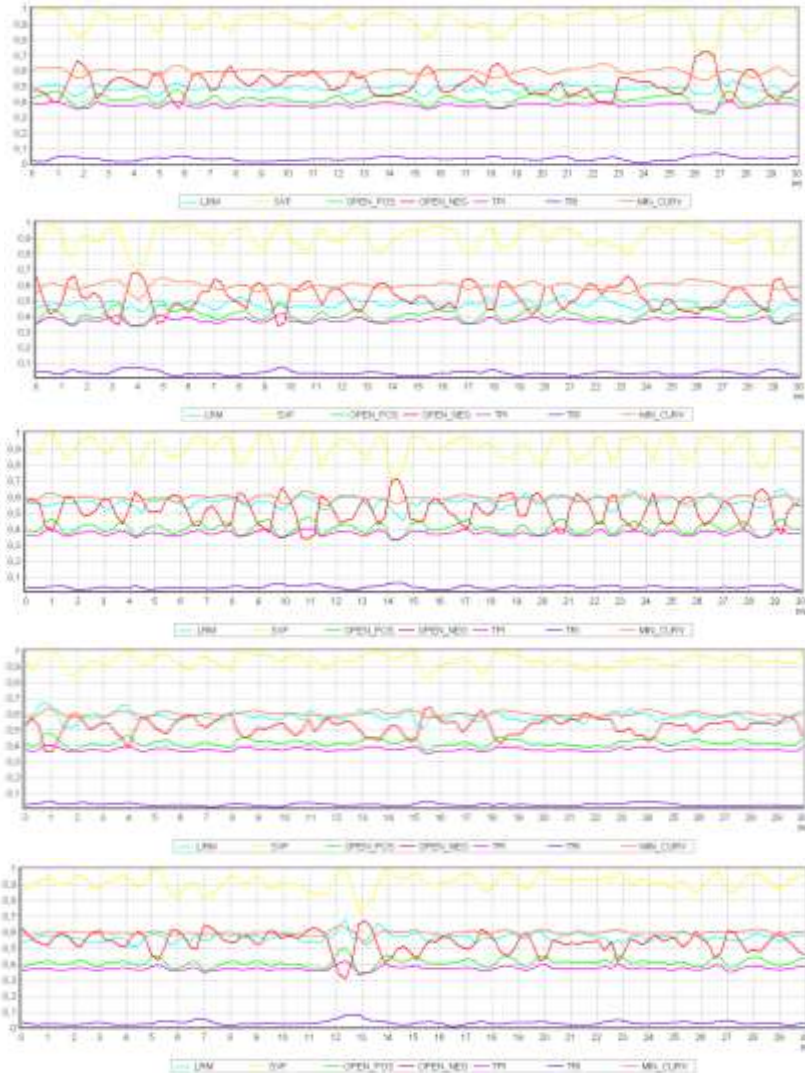


Fig. 22. Comparison of the five profiles along the test line:

- 0. id = 0, made on LRM, SVF, OPEN_POS, OPEN_NEG, TPI, TRI and MIN_CURV images
- 1. id = 1 made on LRM, SVF, OPEN_POS, OPEN_NEG, TPI, TRI and MIN_CURV images.
- 2. id = 2 made on LRM, SVF, OPEN_POS, OPEN_NEG, TPI, TRI and MIN_CURV images
- 3. id = 3 made on LRM, SVF, OPEN_POS, OPEN_NEG, TPI, TRI and MIN_CURV images
- 4. id = 4 made on LRM, SVF, OPEN_POS, OPEN_NEG, TPI, TRI and MIN_CURV images

The comparison of profiles made on seven DTM-derivatives showed that the SVF and OPEN_NEG profiles definitely best reflect the shape of furrows in the arable field. These profiles are characterised by the most regular, sinusoidal shape with the highest amplitudes of values. The amplitudes are on average about 0.15 to a maximum of 0.3 (Fig. 22; Profile 1-5).

Profiles generated for the group of images TPI, OPEN_POS, LRM are very similar. Their shape is also sinusoidal, but with much smaller amplitudes, not exceeding 0.1 (Fig. 22. Profiles 1-5).

The profiles of the other two images, MIN_CURV and TRI, are the flattest and the least regular. The appearing amplitudes reach values of about 0.05 (Fig. 22; Profiles 1-5).

Automatic detection of ploughing traces and its evaluation

DTM derivatives were subjected to the process of automatic detection of ploughing traces. The upper and lower test area in the range shown in Figure 5. allow for a visual comparison of the examined images. However, these fields are too small to properly verify the automatic detection. The arable fields cover virtually the entire upper test area, and it would be difficult to evaluate the results of image filtration. For this reason, it was decided to enlarge the test fields (Fig. 23). The upper and lower test fields are squares with sides approximately 500 meters and 250 meters long.

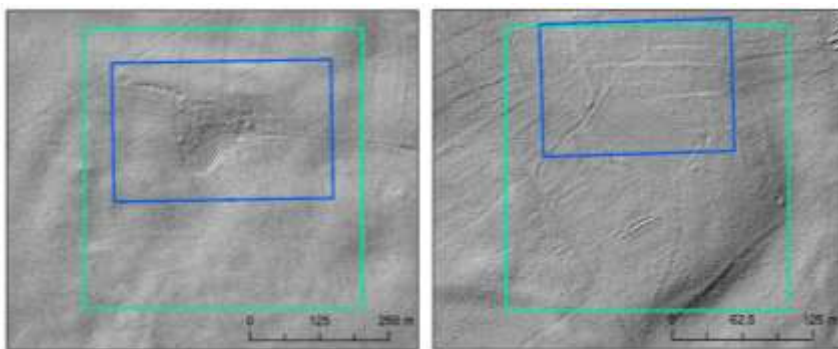


Fig. 23. Top (left) and bottom (right) test field. Blue - the range of the test fields for visual comparison, green - the range of the test fields for automatic detection of ploughing traces

In general, the process of automatic detection of arable field tracks consisted of the following stages:

- Filtering images with a median filter to eliminate noise [50];
- Thresholding and filtering with the Sobel filter for edge detection [51];
- Dilating, eroding and re-dilating to highlight ploughed areas [52];
- Selecting areas larger than 5000 pixels, i.e., about 300m², in order to eliminate small areas.

The method is simple, quick to calculate, and gives good results. All the above activities were performed in the Matlab environment. The image filtering results are presented in (Fig. 25. and 26.). These are binary images, where the value 1 (white) indicates arable fields, and the value 0 (black) indicates the rest of the area.

By comparing visually, the obtained results of image filtration with the manual vectorisation of the boundaries of arable fields (Fig. 24) it can be seen that in the case of the upper test field (Fig. 25), the most traces of ploughing were detected on the Openness Negative, Openness Positive and TPI images, fewer traces can be seen on the Sky View Factor and Minimum Curvature images, and the fewest traces are visible in LRM and TRI. Unfortunately, in virtually every image, a certain group of pixels has been misclassified as arable field. The number of misclassified pixels increases when more traces of ploughing are detected in an image. In the visual assessment, the best detection effects were obtained on the TPI image.

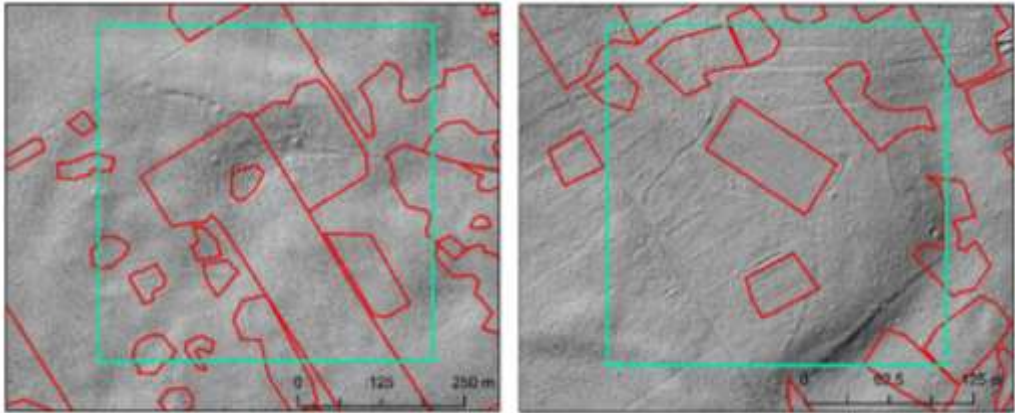


Fig. 24. Manual vectorisation of ploughing traces (red) on the top (left) and bottom (right) test fields.

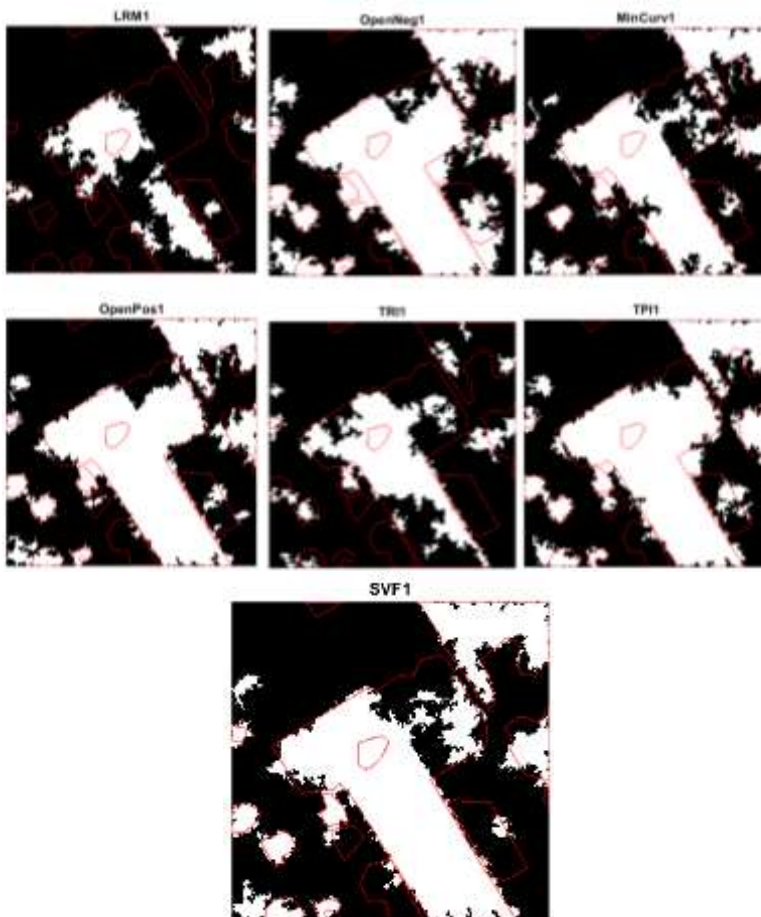


Fig. 25. The upper test fields. The result of the automatic detection of ploughing traces (white colour). The borders of the fields vectorised by the operator are shown in red

In the case of the bottom test field (Fig. 26), it is very difficult to indicate which images were best classified. The largest number of correctly classified pixels was obtained in the

Openness Negative, TRI, Openness Positive, TPI, SVF and Minimum Curvature images. Only the classification made on the LRM image differs significantly from the others. In this image, the fewest pixels have been correctly classified. In the lower test field, there are places where the filtration highlights objects that are not traces of ploughing. These are a forest road, running on the left side from north to south, and the slope of the hill, running on the right side, in an arc from east to south.

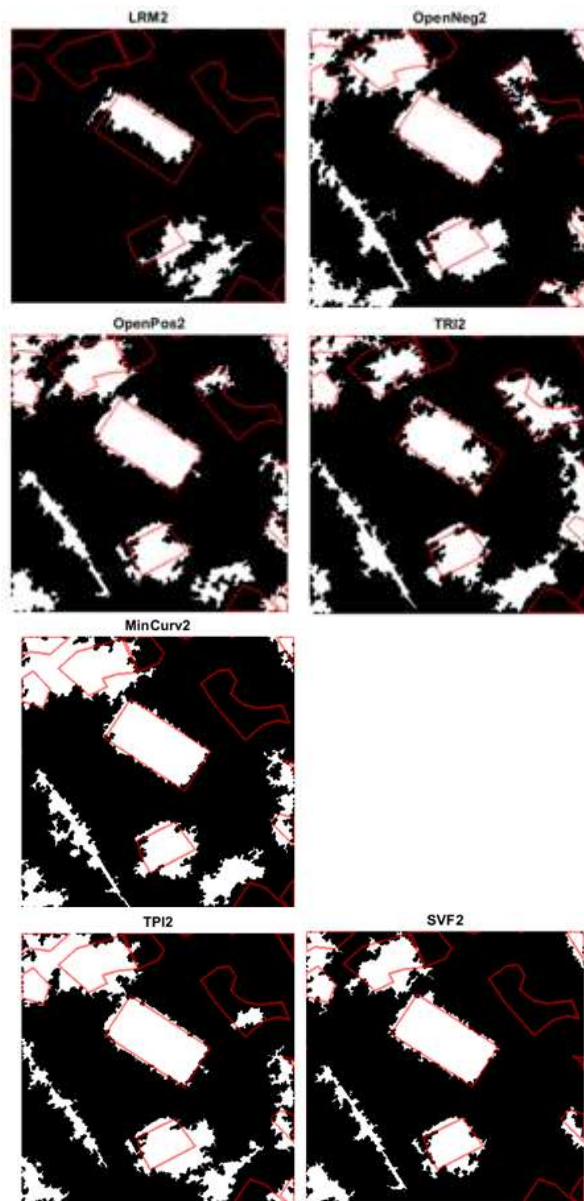


Fig. 26. The lower test fields. The result of the automatic detection of ploughing traces (white colour). The borders of the fields vectorised by the operator are shown in red

The above observations confirm the results of the classification evaluation carried out with the use of the Kappa coefficient [53]. Table 3 shows the results of the classification assessment for the top and bottom test fields. The classifier's accuracy shows false positives

where pixels are incorrectly classified as a known class when they should have been classified as something else. The Total row shows the number of points that should have been identified as a given class, according to the ground truth data. The operator’s accuracy is a false negative where pixels of a known class are classified as something other than that class. The Total column shows the number of points that were identified as a given class, according to the classified map. The classification evaluation was performed in the ArcGIS software.

Table 3. Classification evaluation results for the top (left) and bottom (right) test fields

TPI	OPERATOR		Total	Accuracy	Kappa
Class Value	C_0	C_1			
C_0	1 887 450	371 986	2 259 436	0.84	0.70
C_1	223 140	1 517 424	1 740 564	0.87	
Total	2 110 590	1 889 410	4 000 000	-	
Accuracy	0.89	0.80	-	0.85	

TPI	OPERATOR		Total	Accuracy	Kappa
Class Value	C_0	C_1			
C_0	677 640	64 715	742 355	0.91	0.48
C_1	119 731	137 914	257 645	0.54	
Total	797 371	202 629	1 000 000	-	
Accuracy	0.85	0.68	-	0.82	

Openness Positive

Class Value	C_0	C_1	Total	Accuracy	Kappa
C_0	1 917 230	421 179	2 338 409	0.82	0.69
C_1	193 414	1 468 177	1 661 591	0.88	
Total	2 110 644	1 889 356	4 000 000	-	
Accuracy	0.91	0.78	-	0.85	

Openness Positive

Class Value	C_0	C_1	Total	Accuracy	Kappa
C_0	697 727	66 534	764 261	0.91	0.52
C_1	99 610	136 129	235 739	0.58	
Total	797 337	202 663	1 000 000	-	
Accuracy	0.88	0.67	-	0.83	

Openness Negative

Class Value	C_0	C_1	Total	Accuracy	Kappa
C_0	1 773 749	319 012	2 092 761	0.85	0.67
C_1	336 873	1 570 366	1 907 239	0.82	
Total	2 110 622	1 889 378	4 000 000	-	
Accuracy	0.84	0.83	-	0.84	

Openness Negative

Class Value	C_0	C_1	Total	Accuracy	Kappa
C_0	684 616	52 093	736 709	0.93	0.54
C_1	112 732	150 559	263 291	0.57	
Total	797 348	202 652	1 000 000	-	
Accuracy	0.86	0.74	-	0.84	

Sky View Factor

Class Value	C_0	C_1	Total	Accuracy	Kappa
C_0	1 956 735	571 212	2 527 947	0.77	0.63
C_1	153 875	1 318 178	1 472 053	0.90	
Total	2 110 610	1 889 390	4 000 000	-	
Accuracy	0.93	0.70	-	0.82	

Sky View Factor

Class Value	C_0	C_1	Total	Accuracy	Kappa
C_0	732 451	80 292	812 743	0.90	0.54
C_1	64 906	122 351	187 257	0.65	
Total	797 357	202 643	1 000 000	-	
Accuracy	0.92	0.60	-	0.85	

C L A S S I F I E R

Minimum Curvature

Class Value	C_0	C_1	Total	Accuracy	Kappa
C_0	1 945 754	623 227	2 568 981	0.76	0.60
C_1	164 890	1 266 129	1 431 019	0.88	
Total	2 110 644	1 889 356	4 000 000	-	
Accuracy	0.92	0.67	-	0.80	

Minimum Curvature

Class Value	C_0	C_1	Total	Accuracy	Kappa
C_0	672 851	69 804	742 655	0.91	0.45
C_1	124 530	132 815	257 345	0.52	
Total	797 381	202 619	1 000 000	-	
Accuracy	0.84	0.66	-	0.81	

TRI

Class Value	C_0	C_1	Total	Accuracy	Kappa
C_0	2 002 451	1 183 724	3 186 175	0.63	0.33
C_1	108 163	705 662	813 825	0.87	
Total	2 110 614	1 889 386	4 000 000	-	
Accuracy	0.95	0.37	-	0.68	

TRI

Class Value	C_0	C_1	Total	Accuracy	Kappa
C_0	690 528	79 020	769 548	0.90	0.45
C_1	106 804	123 648	230 452	0.54	
Total	797 332	202 668	1 000 000	-	
Accuracy	0.87	0.61	-	0.81	

Local Relief Model

Class Value	C_0	C_1	Total	Accuracy	Kappa
C_0	2 064 334	1 298 123	3 362 457	0.61	0.30
C_1	46 263	591 280	637 543	0.93	
Total	2 110 597	1 889 403	4 000 000	-	
Accuracy	0.98	0.31	-	0.66	

Local Relief Model

Class Value	C_0	C_1	Total	Accuracy	Kappa
C_0	759 763	162 718	922 481	0.82	0.19
C_1	37 570	39 949	77 519	0.52	
Total	797 333	202 667	1 000 000	-	
Accuracy	0.95	0.20	-	0.80	

The Kappa coefficient may take values in the range $<-1; 1>$. Negative values mean that the agreement of the evaluators (automaton and operator) is lower than the chance of their coincidence, i.e., no match. The 0 values are the rates agreement at a random agreement level. Values above 0 are commonly interpreted on the basis of a comparative scale (Table 4.) developed by Landis and Koch [54].

Table 4. Interpretation of the values taken by the Kappa coefficient according to Landis and Koch

Kappa	Strength of Agreement
<0.00	Poor
0.00-0.20	Slight
0.21-0.40	Fair
0.41-0.60	Moderate
0.61-0.80	Substantial
0.81-1.00	Almost Perfect

The upper test field was best classified (at the Substantial level) on the images: TPI (Kappa = 0.70), Openness Positive (Kappa = 0.69), Openness Negative (Kappa = 0.67), Sky-View Factor (Kappa = 0.63). At the Moderate level - Minimum Curvature (Kappa = 0.60). The lowest score, at the Fair level, was the classification on the TRI (Kappa = 0.33) and LRM (Kappa = 0.30) images.

The lower test field was classified in almost all images at the Moderate level: Sky View Factor (Kappa = 0.54), Openness Negative (Kappa = 0.54), Openness Positive (Kappa = 0.52), TPI (Kappa = 0.8), Minimum Curvature (Kappa = 0.45), TRI (Kappa = 0.45). The exception is the LRM image (Kappa = 0.19), where the strength of agreement is at the Slight level.

Given the results obtained for the lower test field, a much lower accuracy was obtained than for the upper test field. This is due to the fact that the Kappa coefficient is sensitive to changes in the distribution of values for pairs of consistent 0-0 and 1-1 decisions. The greater the concentration of scores in one of the cells for pairs of 0-0 or 1-1 cases, the lower the value of the Kappa coefficient. On the other hand, "shifting" the results of observations for pairs 0-1 and 1-0 has no major impact on its value. In the case of the upper test field, the distribution of 0 and 1 in the reference image (classified by the operator) is even (50/50). In the case of the lower test field, in the reference class there is a large concentration of pixels around the value of 0 (80% of all pixels). Hence the supposition that the Kappa coefficient would have had a higher value, had it not been for the specificity of this image.

Conclusions

Identification of ploughing traces in forested areas with the use of ALS provides a wide testing ground. This article proposes the use of DTM derivatives (built on the basis of data from ALS) to detect sites where ploughing has been recently performed. By "recently" it is meant up to 10 years ago.

First, as a part of the research, the following algorithms were parameterised with the use of the field profiles Local Relief Model, Sky-View Factor, Openness Positive, Openness Negative, Topographic Position Index, Morphometric Features - Minimum Curvature, and Terrain Ruggedness Index. The comparison of the profiles allowed for the selection of the best parameter values for each algorithm. On their basis, seven DTM-derived images were generated that best represented arable fields.

Subsequent work included a visual comparison of the derived images and the comparison of t profiles made along five test lines on each of the images. This allowed for the selection of images with the clearest traces of ploughed fields. SVF and Openness negative

images turned out to be the best in this case. Then, automatic detection of ploughing traces was performed with the use of morphological filters. The detection results were compared with the manually vetted borders of arable fields. At this stage, in terms of the visual assessment, the results were satisfactory. Nevertheless, an evaluation of the classification was also done using the Kappa coefficient. Substantial and Moderate levels were obtained for the Topographic Position Index, Openness Positive, Openness Negative, Sky-View Factor, and Minimum Curvature images. The classification in the Terrain Ruggedness Index image (Moderate / Fair level) was assessed worse, and the lowest rating was obtained by the classification in the Local Relief Model image (Fair/Slight level).

The article attempts to diagnose the problem of identifying traces of forest crops within potential archaeological sites. By analysing the images of DTM derivatives, it is possible to indicate the images of Openness Positive, Openness Negative, Sky-View Factor as well as those in which field microforms, such as ploughing traces, are best presented. Their use will allow the operator to easily indicate places of forest cultivation.

To automate the process of detecting farmland, it is also worth using the Openness Positive, Openness Negative, Sky-View Factor and Topographic Position Index images. On their basis, the filtering of the images shows the places of ploughing traces at a satisfactory level. It is worth noting that a relatively simple and fast method based on morphological filters was used for automatic detection. The use of more complex methods here, such as Gabor's textural filters or a supervised classification, could give better results for automatic detection of ploughing traces. This will be the subject of further research.

The conducted research shows that it is possible to select places in forested areas with traces of ploughing both manually and automatically. Such identification is extremely important not only in the process of deconstruction and isolation of landscape features, but it is also significant from the point of view of conducting prospective and verification research in the field. The results of the analyses showing the traces of ploughing will be helpful in terms of research planning and assessing its effectiveness in difficult forest terrains. A comparison of the obtained results with potential archaeological sites will show archaeologists the location for field research.

Acknowledgements

This paper was made at AGH-UST within statutory research 16.16.150.545

References

- [1] B.J. Devereux, G.S. Amable, P. Crow, A.D. Cliff, *The potential of airborne lidar for detection of archaeological features under woodland canopies*, **Antiquity**, **79**, 2005, pp. 648–660. <https://doi.org/10.1017/S0003598X00114589>.
- [2] M. Doneus, C. Briese, *Airborne Laser Scanning in Forested Areas - Potential and Limitations of an Archaeological Prospection Technique*, **Remote Sensing for Archaeological Heritage Management: Proceedings of the 11th EAC Heritage Management Symposium, Reykjavík, Iceland, 25-27 March 2010**, pp. 59–71.
- [3] R. Hesse, *The changing picture of archaeological landscapes: lidar prospection over very large areas as part of a cultural heritage strategy*, **Interpreting Archaeological Topography. Airborne Laser Scanning, 3D Data and Ground Observation** (Editors: R.B. Opiz, D.C. Cowley), Oxbow Books, 2013, pp. 171–183.
- [4] O. Risbøl, O.M. Bollandsås, A. Nesbakken, H.O. Orka, E. Næsset, T. Gobakken, *Interpreting cultural remains in airborne laser scanning generated digital terrain models:*

- Effects of size and shape on detection success rates*, **Jornal of Archaeological Science** **40**(12), 2013, pp. 4688–4700, <https://doi.org/10.1016/j.jas.2013.07.002>.
- [5] B. Sittler, *Revealing Historical Landscapes by Using Airborne Laser Scanning - A 3D Modell of Ridge and Furrow in Forests Near Rastatt (Germany)*, **International Archives of Photogrammetry, Remote Sensing and Spatial Information Sciences** **36**(8), 2004, pp. 258–261. <https://www.isprs.org/proceedings/XXXVI/8-W2/SITTLER.pdf>.
- [6] R. Bennett, K. Welham, R. a. Hill, A. Ford, *A Comparison of Visualization Techniques for Models Created from Airborne Laser Scanned Data*, **Archaeological Prospection** **19**(1), 2012, pp. 41–48. <https://doi.org/10.1002/arp.1414>.
- [7] B.J. Devereux, G.S. Amable, P. Crow, *Visualisation of LiDAR terrain models for archaeological feature detection*, **Antiquity**, **82**(316), 2008, pp. 470–479. <https://doi.org/10.1017/S0003598X00096952>.
- [8] B. Štular, Ž. Kokalj, K. Oštir, L. Nuninger, *Visualization of lidar-derived relief models for detection of archaeological features*, **Journal of Archaeological Science** **39**(11), 2012, pp. 3354–3360. <https://doi.org/10.1016/j.jas.2012.05.029>.
- [9] R. Hesse, *LiDAR-derived Local Relief Models - a new tool for archaeological prospection*, **Archaeological Prospection** **17**(2), 2010, pp. 67–72. <https://doi.org/10.1002/arp.374>.
- [10] Ž. Kokalj, K. Zakšek, K. Oštir, *Application of sky-view factor for the visualisation of historic landscape features in lidar-derived relief models*, **Antiquity**, **85**(327), 2011, pp. 263–273. <https://doi.org/10.1017/S0003598X00067594>.
- [11] K. Zakšek, K. Oštir, Ž. Kokalj, *Sky-View Factor as a Relief Visualization Technique*, **Remote Sens.** **3**(2), 2011, pp. 398–415. <https://doi.org/10.3390/rs3020398>.
- [12] M. Doneus, *Openness as Visualization Technique for Interpretative Mapping of Airborne Lidar Derived Digital Terrain Models*, **Remote Sensing** **5**(12), 2013, pp. 6427–6442. <https://doi.org/10.3390/rs5126427>.
- [13] A.D. Weiss, *Topographic Position and Landforms Analysis*, **Poster**, 2001.
- [14] J. Wood, **The geomorphological characterisation of Digital Elevation Models**, University of Leicester, 1996. https://leicester.figshare.com/articles/thesis/The_geomorphological_characterisation_of_Digital_Elevation_Models_/10152368.
- [15] J. Wood, *Geomorphometry in LandSerf*, Elsevier, 2009, pp. 333–349. [https://doi.org/10.1016/S0166-2481\(08\)00014-7](https://doi.org/10.1016/S0166-2481(08)00014-7).
- [16] S.J. Riley, S.D. DeGloria, R. Elliot, *A Terrain Ruggedness Index that quantifies topographic heterogeneity*, **Intermountain Journal of Sciences** **5**(1-4), 1999, pp. 23–27. http://download.osgeo.org/qgis/doc/reference-docs/Terrain_Ruggedness_Index.pdf (accessed February 15, 2021).
- [17] D. Mlekuž, *Skin Deep: LiDAR and Good Practice of Landscape Archaeology*, **Good Practice in Archaeological Diagnostics. Non-invasive Survey of Complex Archaeological Sites** (Editors C. Corsi, B. Slapšak, F. Vermeulen), 2013, pp. 113–129. https://doi.org/10.1007/978-3-319-01784-6_6.
- [18] K.M. Johnson, W.B. Ouimet, *An observational and theoretical framework for interpreting the landscape palimpsest through airborne LiDAR*, **Applied Geography** **91**, 2018, pp. 32–44. <https://doi.org/10.1016/j.apgeog.2017.12.018>.
- [19] P.J. Crutzen, *The “Anthropocene,”*, **Earth System Science in the Anthropocene. Emerging Issues and Problems** (Editors E. Ehlers, T. Krafft), Springer-Verlag, Berlin/Heidelberg, 2006, pp. 13–18. https://doi.org/10.1007/3-540-26590-2_3.
- [20] R. Hesse, *Detecting former field systems with airborne LIDAR - an overview of current methods*, **Aerial Archaeology, Remote Sensing and Archaeological Process (AARG) Conference 2012, 13th-15th September, Budapest, Hungary 2012**, poster.

- https://www.academia.edu/1941481/Detecting_former_field_systems_with_airborne_LID_AR_an_overview_of_current_methods.
- [21] F. Welc, J. Nitychoruk, R. Solecki, K. Rabięga, J. Wysocki, *Results of Integrated Geoarchaeological Prospection of Unique Iron Age Hillfort Located on Radomno Lake Island in North-Eastern Poland*, **Studia Quaternaria** **35**(1), 2018, pp. 55–71. DOI: 10.2478/squa-2018-0004.
- [22] M. Sosnowski, A.M. Noryskiewicz, J. Czerniec, *Examining a scallop shell-shaped plate from the Late Roman Period discovered in Osie* (site no.: Osie 28, AZP 27-41/26), northern Poland, **Analecta Archaeologica Ressoviensia** **14**, 2019, pp. 91–98. <https://doi.org/10.15584/anarres.2019.14.7>.
- [23] G. Lambrick, **The management of archaeological sites in arable landscapes**, London, 2004. <http://sciencesearch.defra.gov.uk/Default.aspx?Menu=Menu&Module=More&Location=None&Completed=0&ProjectID=8412>.
- [24] K. Challis, P. Forlin, M. Kinsey, *A Generic Toolkit for the Visualization of Archaeological Features on Airborne LiDAR Elevation Data*, **Archaeological Prospection** **18**(4), 2011, pp. 279–289. <https://doi.org/10.1002/arp.421>.
- [25] Ž. Kokalj, K. Oštir, *Lidar Data Visualization and Processing*, **The Encyclopedia of Archaeological Sciences** (Editor S.L. López Varela), John Wiley & Sons, Inc., Hoboken, NJ, USA, 2018, pp. 1–6. <https://doi.org/10.1002/9781119188230.saseas0347>.
- [26] Ž. Kokalj, M. Somrak, *Why Not a Single Image? Combining Visualizations to Facilitate Fieldwork and On-Screen Mapping*, **Remote Sensing** **11**(7), 2019, article number: 747. <https://doi.org/10.3390/rs11070747>.
- [27] A. Guisan, S.B. Weiss, A.D. Weiss, *GLM versus CCA spatial modeling of plant species distribution*, **Plant Ecology** **143**, 1999, pp. 107–122. <https://doi.org/10.1023/A:1009841519580>.
- [28] J. Jenness, **Topographic Position Index (tpi_jen.avx) extension for ArcView 3.x, v. 1.2**, 2006. Jenness Enterprises. Available at: <http://www.jennessent.com/arcview/tpi.htm>.
- [29] P.G. Vinod, *Development of topographic position index based on Jenness algorithm for precision agriculture at Kerala, India*, **Spatial Information Research** **25**, 2017, pp. 381–388. <https://doi.org/10.1007/s41324-017-0104-8>.
- [30] M. Setiawan, M. Rutzinger, V. Wichmann, J. Stoetter, J. Sartohadi, *Evaluation of methods for digital elevation model interpolation of tillage systems*, **Journal of Natural Resources and Development**, **3**, 2013, pp. 128–139. <https://doi.org/10.5027/jnrd.v3i0.13>.
- [31] N. Poirier, R. Opitz, L. Nuninger, K. Ostir, *Lidar in Mediterranean agricultural landscapes*, **Interpreting Archaeological Topography: 3D Data, Visualisation and Observation** (Editors: R.S. Opitz, D.C. Cowley), Oxbow Books, 2013, pp. 184–196. <https://doi.org/10.2307/j.ctvh1dqdz.20>.
- [32] Archiwum Map Zachodniej Polski, (n.d.). <http://mapy.amzp.pl/> (accessed June 1, 2021).
- [33] Informatyczny System Osłony Kraju, (n.d.). <https://isok.gov.pl/> (accessed February 20, 2021).
- [34] D. Novák, *Local Relief Model (LRM) Toolbox for ArcGIS* (UPDATE 2016-05 - new download link), (2014). <https://doi.org/10.13140/RG.2.1.2010.1201/1>.
- [35] G. Kierszys, Ł. Banaszek, *Dostrzec i zrozumieć. Porównanie wybranych metod wizualizacji danych ALS wykorzystywanych w archeologii*, **Folia Praehistorica Posnaniensia** **22**, 2018, pp. 233–270. <https://doi.org/10.14746/fpp.2017.22.11>.
- [36] D.G. Steyn, *The calculation of view factors from fisheye-lens photographs: Research note*, **Atmosphere-Ocean** **18**(3), 1980, pp. 254–258. <https://doi.org/10.1080/07055900.1980.9649091>.

- [37] J. Dozier, J. Bruno, P. Downey, *A faster solution to the horizon problem*, **Computers & Geosciences** 7(2), 1981, pp. 145–151. [https://doi.org/10.1016/0098-3004\(81\)90026-1](https://doi.org/10.1016/0098-3004(81)90026-1).
- [38] R. Yokoyama, M. Shirasawa, R. Pike, *Visualizing Topography by Openness: A New Application of Image Processing to Digital Elevation Models*, **Photogrammetric Engineering & Remote Sensing** 68(3), 2002, pp. 257–266.
- [39] I.S. Evans, *An integrated system of terrain analysis and slope mapping*, University of Durham, Durham, 1980.
- [40] L.W. Zevenbergen, C.R. Thorne, *Quantitative analysis of land surface topography*, **Earth Surface Processes and Landforms** 12(1), 1987, pp. 47–56. <https://doi.org/10.1002/esp.3290120107>.
- [41] P.A. Shary, *Land surface in gravity points classification by a complete system of curvatures*, **Mathematical Geology** 27, 1995, pp. 373–390. <https://doi.org/10.1007/BF02084608>.
- [42] Q. Wu, Y. Chen, H. Zhou, S. Chen, H. Wang, *A New Algorithm for Calculating the Flow Path Curvature (C) from the Square-Grid Digital Elevation Model (DEM)*, **International Journal of Geo-Information** 9(9), 2020, article number: 510. <https://doi.org/10.3390/ijgi9090510>.
- [43] I.V. Florinsky, *Accuracy of local topographic variables derived from digital elevation models*, **International Journal of Geographical Information Science** 12(1), 1998, pp. 47–62. <https://doi.org/10.1080/136588198242003>.
- [44] I.V. Florinsky, *Combined analysis of digital terrain models and remotely sensed data in landscape investigations*, **Progress in Physical Geography: Earth and Environment** 22(1), 1998, pp. 33–60. <https://doi.org/10.1177/030913339802200102>.
- [45] J. Schmidt, I.S. Evans, J. Brinkmann, *Comparison of polynomial models for land surface curvature calculation*, **International Journal of Geographical Information Science** 17(8), 2003, pp. 797–814. <https://doi.org/10.1080/13658810310001596058>.
- [46] M. Różycka, P. Migoń, A. Michniewicz, *Topographic Wetness Index and Terrain Ruggedness Index in geomorphic characterisation of landslide terrains, on examples from the Sudetes, SW Poland*, **Zeitschrift Für Geomorphologie** 61(2), 2017, pp. 61–80. https://doi.org/10.1127/zfg_suppl/2016/0328.
- [47] S. Mukherjee, S. Mukherjee, R.D. Garg, A. Bhardwaj, P.L.N. Raju, *Evaluation of topographic index in relation to terrain roughness and DEM grid spacing*, **Journal of Earth System Science** 122, 2013, pp. 869–886. <https://doi.org/10.1007/s12040-013-0292-0>.
- [48] M. Moreno, S. Levachkine, M. Torres, R. Quintero, *Geomorphometric analysis of raster image data to detect terrain ruggedness and drainage density*, **Progress in Pattern Recognition, Speech and Image Analysis. CIARP 2003. Lecture Notes in Computer Science** (Editors: Sanfeliu, A., Ruiz-Shulcloper, J.), vol. 2905, Springer, Berlin, Heidelberg, 2003, pp. 643–650. https://doi.org/10.1007/978-3-540-24586-5_79.
- [49] T. Verbovšek, T. Popit, *Analysis of surface roughness in the Sveta Magdalena paleo-landslide in the Rebrnice area*, **RMZ-M&G** 60, 2013, pp. 197–204.
- [50] A. Shah, J.I. Bangash, A.W. Khan, I. Ahmed, A. Khan, A. Khan, A. Khan, *Comparative analysis of median filter and its variants for removal of impulse noise from gray scale images*, **Journal of King Saud University - Computer and Information Science** 34(3), 2020, pp. 505–519. <https://doi.org/10.1016/j.jksuci.2020.03.007>.
- [51] G. Ravivarma, K. Gavaskar, D. Malathi, K.G. Asha, B. Ashok, S. Aarthi, *Implementation of Sobel operator based image edge detection on FPGA*, **Materials Today: Proceedings** 45(2), 2021, pp. 2401–2407. <https://doi.org/10.1016/j.matpr.2020.10.825>.
- [52] S. Lou, X. Jiang, P.J. Scott, *Geometric computation theory for morphological filtering on*

- freeform surfaces*, **Proceedings of the Royal Society A. Mathematical, Physical and Engineering Science** **469**(2159), 2013, article number: 20130150. <https://doi.org/10.1098/rspa.2013.0150>.
- [53] J. Cohen, *A Coefficient of Agreement for Nominal Scales*, **Educational and Psychological Measurement** **20**(1), 1960, pp. 37–46. <https://doi.org/10.1177/001316446002000104>.
- [54] J.R. Landis, G.G. Koch, *The Measurement of Observer Agreement for Categorical Data*, **Biometrics** **33**(1), 1977, pp. 159-174. <https://doi.org/10.2307/2529310>.
-

Received: July 13, 2022

Accepted: January 28, 2023